

## MIT Open Access Articles

*Design principles for self-forming interfaces  
enabling stable lithium-metal anodes*

The MIT Faculty has made this article openly available. **Please share**  
how this access benefits you. Your story matters.

**Citation:** Zhu, Yingying, Pande, Vikram, Li, Linsen, Wen, Bohua, Pan, Menghsuan Sam et al. 2020. "Design principles for self-forming interfaces enabling stable lithium-metal anodes." Proceedings of the National Academy of Sciences of the United States of America, 117 (44).

**As Published:** 10.1073/PNAS.2001923117

**Publisher:** Proceedings of the National Academy of Sciences

**Persistent URL:** <https://hdl.handle.net/1721.1/142491>

**Version:** Final published version: final published article, as it appeared in a journal, conference proceedings, or other formally published context

**Terms of Use:** Article is made available in accordance with the publisher's policy and may be subject to US copyright law. Please refer to the publisher's site for terms of use.



OPEN ACCESS

## Mesoscale Model for Ostwald Ripening of Catalyst Nanoparticles

To cite this article: Giovanna Bucci *et al* 2021 *J. Electrochem. Soc.* **168** 054515

View the [article online](#) for updates and enhancements.

**Measure the electrode expansion in the nanometer range.**  
**Discover the new electrochemical dilatometer ECD-4-nano!**

**EL-CELL<sup>®</sup>**  
electrochemical test equipment



- PAT series test cell for dilatometric analysis (expansion of electrodes)
- Capacitive displacement sensor (range 250  $\mu\text{m}$ , resolution  $\leq 5$  nm)
- Optimized sealing concept for high cycling stability

[www.el-cell.com](http://www.el-cell.com) +49 (0) 40 79012 737 [sales@el-cell.com](mailto:sales@el-cell.com)





# Mesoscale Model for Ostwald Ripening of Catalyst Nanoparticles

Giovanna Bucci,<sup>1,z</sup> Karim Gadelrab,<sup>2</sup> and W. Craig Carter<sup>3</sup>

<sup>1</sup>Robert Bosch LLC, Sunnyvale, California 94085, United States of America

<sup>2</sup>Robert Bosch LLC, Cambridge, Massachusetts 02139, United States of America

<sup>3</sup>Department of Materials Science and Engineering, Massachusetts Institute of Technology, Cambridge, Massachusetts 02139, United States of America

A mesoscale model is proposed to characterize coarsening of platinum-based catalyst particles with the aim of understanding cathode degradation and power loss in proton exchange membrane fuel cells (PEMFC). The microstructure of a cathode catalyst layer is more complex than the ones typically described by Ostwald-ripening models, such as the Lifshitz and Slyozov and Wagner (LSW) theory or diffuse interface models. Our model captures the dissolution kinetics of the catalyst material, and the diffusivity of the ions in solution. The network structure of the model embeds the tortuosity of the microstructure and the effect of water content on Pt-ion mobility. Detailed diffusional interactions among catalyst particles are explicitly described with the aim of providing statistically averaged properties of coarsening ensembles. Through numerical tests, the scaling of coarsening kinetics is predicted as function of voltage. The effect of voltage cycling, and initial particle size distribution are also probed. The power-law exponents for the mean square radius vs time are affected by the reduced dimensionality of inter-particle diffusion, constrained by the carbon support and the surface wetting. This theoretical framework can be used to understand how material design influences the degradation pathways that are responsible for platinum surface area loss.

© 2021 The Author(s). Published on behalf of The Electrochemical Society by IOP Publishing Limited. This is an open access article distributed under the terms of the Creative Commons Attribution Non-Commercial No Derivatives 4.0 License (CC BY-NC-ND, <http://creativecommons.org/licenses/by-nc-nd/4.0/>), which permits non-commercial reuse, distribution, and reproduction in any medium, provided the original work is not changed in any way and is properly cited. For permission for commercial reuse, please email: [permissions@iopublishing.org](mailto:permissions@iopublishing.org). [DOI: 10.1149/1945-7111/abf970]



Manuscript submitted January 15, 2021; revised manuscript received March 29, 2021. Published May 11, 2021. *This paper is part of the JES Focus Issue on Proton Exchange Membrane Fuel Cell and Proton Exchange Membrane Water Electrolyzer Durability.*

Proton exchange membrane fuel cells (PEMFC) are increasingly regarded as an alternative for combustion engines in the transportation sector.<sup>1</sup> Despite decades of development, cost and durability remain major barriers to automotive wide market acceptance.<sup>2</sup> If used in vehicles, PEMFCs must be able to withstand thousands of operating hours under changing load conditions.<sup>3</sup> Power loss over the lifetime is mainly caused by the loss of the electrochemically active electrode surface area (ECSA) of the cathode catalyst layer (CCL).<sup>4</sup>

The catalyst layer typically consists of agglomerates of Pt nanoparticles on a carbon support. A solid electrolyte, such as the perfluorosulfonic acid (PFSA) ionomer, is blended with the catalyst to carry protons to the Pt surface.<sup>5</sup>

The cathode potential typically ranges between 0.6 and 0.95 V, but it can rise temporarily above 1.35 V during startup and shutdown of the vehicles. Under such conditions, platinum displays an electrochemically unstable behavior, resulting in Pt dissolution.<sup>6</sup> Upon voltage cycling, platinum mass loss and redistribution leads to loss in catalytic surface area for oxygen reduction reaction and, as a consequence, the cell power fades.<sup>7</sup> In particular, the electrochemical Ostwald ripening of cathode catalyst particles is responsible for a significant decrease in ECSA.<sup>8</sup> Ostwald ripening, or particle coarsening, is a competitive growth process in which a system lowers its energy by reducing its interfacial area. During coarsening, large particles grow at the expense of small particles. This leads to an increase in the average particle size and a decrease in catalytic surface area.

Smaller particles undergo accelerated dissolution due to their local higher chemical potential (Gibbs-Thompson effect), and Pt-ions are driven from smaller to larger particles due to the chemical-potential gradient.<sup>9</sup> Dissolved ions tend to re-deposit on large particles, leading to permanent particle growth and an increase in the mean particle size (see Fig. 1).

Agglomeration and coalescence can also contribute to the growth of catalyst particles. These processes may occur due to migration and collision of nanoparticles over the surface of the carbon support or to corrosion of the carbon support itself.<sup>2,4,10</sup>

Dissolved platinum can also diffuse into the membrane and become electrochemically inactive after reacting with hydrogen that permeates the membrane from the anode. However, the membrane diffusion-length is on the order several micrometers and is considerably larger than the average inter-particle distance (less than 50 nm<sup>4</sup>).

A complete theory of the coarsening of a system of spherical particles was developed by Lifshitz and Slyozov<sup>11</sup> and by Wagner<sup>12</sup> (the LSW theory). They predicted the existence of a steady-state coarsening state for nearly all initial conditions of the system, wherein: i) under the scaling of the average radius, the particle-radius distribution becomes unique and time independent; ii) for diffusion limited coarsening, the cube of the average radius  $\langle r \rangle^3$  increases linearly with time; iii) the number of particles per unit volume decreases linearly with time. The LSW theory is valid in the limit of a zero volume-fraction of the coarsening phase and in the long-time limit. The time required to reach steady state coarsening depends on properties of the system such as inter-particle diffusivity and capillary length.<sup>13</sup> Under these assumptions, particles interact only indirectly through a mean field provided by the solution matrix. Proximity effects—where the behavior of a particle depends on its neighboring particles—are not captured by the LSW. Proximity effects derive from diffusional interactions and non-zero volume fraction; these are predicted to increase the coarsening rate without altering the temporal power laws predicted by LSW.<sup>14</sup> The effect of diffusional interactions can be expressed through the prefactor  $K(\phi)$  as  $\langle r \rangle^3 = K(\phi)t$ , with  $\phi$  indicating the Pt-volume fraction or the average inter-particle distance.

In the PEM fuel cell aging literature, the evolution of Pt-particles size distribution has been also predicted by the Smoluchowski equation for population balance.<sup>15,16</sup> Most of the literature agrees that Ostwald ripening contributes largely to particle coarsening, while there is no agreement on the contribution of particle migration and coalescence.<sup>4,17</sup> In Refs. 15, 16, the Smoluchowski has been used to predict particle coarsening, without distinction between specific mechanisms.

The LSW theory and the Smoluchowski equation may not predict behavior for real microstructures because they do not account for diffusional interactions between particles. They predict that the coarsening rate of a particle is a function only of its radius relative to the average particle size. However, in nonzero volume

<sup>z</sup>E-mail: [Giovanna.Bucci@us.bosch.com](mailto:Giovanna.Bucci@us.bosch.com); [Giov.bucci@gmail.com](mailto:Giov.bucci@gmail.com)

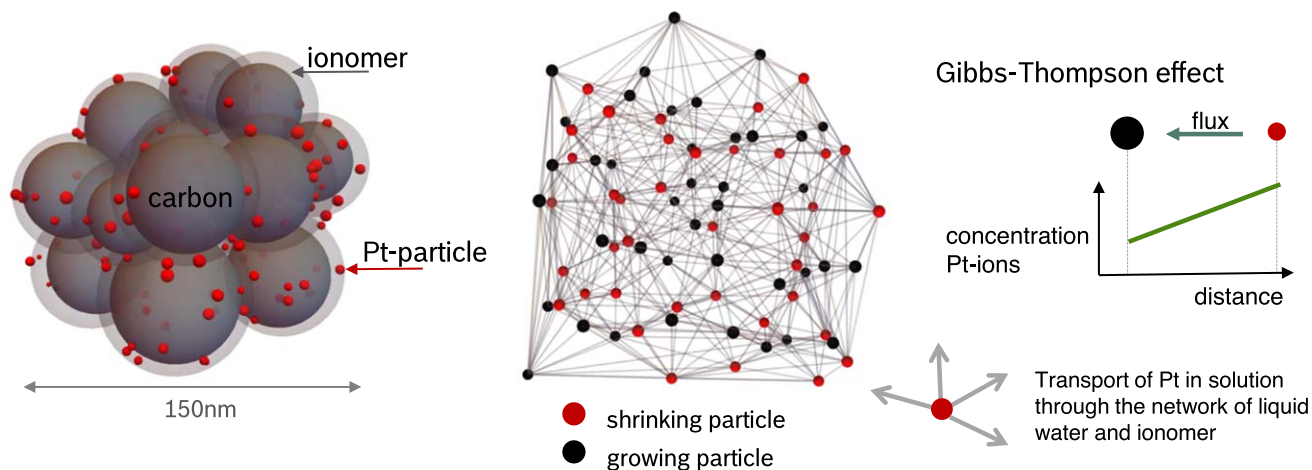


**Figure 1.** The image on the left illustrates the packing of a cathode catalyst layer microstructure based on Vulcan-carbon substrate. The platinum particles (in red) decorate the carbon surface and they are covered by an ionomer layer (gray area). The catalyst particles are connected by a network of liquid water and ionomer that allows for Pt-ion mobility and mass redistribution. (The center image illustrates a subset of the Pt-particles and their 3D connectivity.) Smaller nanoparticles undergo accelerated dissolution due to their local higher chemical potential (Gibbs-Thompson effect). Non-uniform particle size causes a non-uniform concentration of Pt-ions in solution and a flux from smaller to larger particles. Dissolved ions tend to re-deposit on large particles, leading to permanent particle growth and an increase in the mean particle size.

fraction systems, when a particle of a given size is surrounded by particles larger than itself it tends to shrink—regardless of that particle's size compared to the mean. Conversely, if the particle is surrounded by particles that are smaller than itself, it tends to coarsen. This is mostly relevant when the coarsening is diffusion limited and the behaviour of each particle is affected by its nearest neighbours.

Local interactions are especially relevant in the investigation of the role of the carbon support in determining catalyst performance and stability. Furthermore, because Pt-diffusion between particles is restricted to the regions between the carbon particles, the dimensionality of diffusion is reduced and would exaggerate proximity effects. The carbon microstructure provides internal porosity to host Pt-particles and protect them from direct ionomer adsorption, while not-restricting oxygen transport. For instance, in high-surface-carbon materials, the Pt inter-particle distance tends to be large.<sup>4</sup> Also, the pore structures can be used to increase the tortuosity and limit the range of mass redistribution during coarsening. Tortuosity may also exacerbate proximity effects. The retention of capillary water depends on the pore-size. Water filling the carbon pores tend to impede the oxygen reaction and promote Ostwald ripening by providing a medium for Pt-ion mobility.

The microstructure of a cathode catalyst layer is more complex than the ones typically described by Ostwald-ripening models. Diffuse-interface models have been employed to describe solute redistribution processes occurring in two-phase systems, with the coarsening particles embedded in a matrix of supersaturated solution. To overcome the limitations of existing models, we develop a new method with the scope of providing a mesoscale description of the coarsening process and the detailed diffusional interactions among catalyst particles within the cathode microstructure. A mesoscale approach is instrumental to understanding how material design influences the degradation pathways that are responsible for the macroscopically observed platinum surface area loss. This theoretical framework can be used to determine the coarsening rate of individual particles, in addition to providing statistically averaged properties of coarsening ensembles that are experimentally accessible. In this paper, we describe the model and demonstrate its use for a particular microstructure. The model could be applied to other systems and geometries. The model captures two main phenomena: the dissolution kinetics of the catalyst material, and the diffusivity of the ions in solution. The diffusivity depends on the

tortuosity of the microstructure and on the liquid water content, and therefore the relative humidity during operation. Electrochemical reactions of Pt adsorption/desorption, and diffusion around the surface layer are also encoded in the model.

In PEMFC cathodes, Pt-ion diffusion and Pt-mass redistribution among particles is mediated by a network of liquid water and ionomer. This diffusional network depends on the porosity of the microstructure, on its wetting properties, and on the operating conditions, particularly the relative humidity and the applied current. The proposed mesoscale model is able to capture such complexity through a 3-dimensional network of diffusion pathways connecting the catalyst particles. The network represents the particle locations and the effective inter-particle distance, it can also embed local variations of surface kinetics and diffusion properties. Transient water-saturation conditions and long term changes in surface hydrophobic properties can be incorporated by evolving the model parameters over each voltage cycle or over the lifetime of the cell. The inter-particle distance changes over time due to coarsening but also as a consequence of carbon corrosion. Carbon corrosion tends to weaken the particles attachment and it is a possible cause of agglomeration. Depending on its severity, it can alter the structural integrity of the support and increase the tortuosity of the microstructure.

## Model

**Data structure.**—The network model consists of three elements: vertex, satellite and edge (see Fig. 2). A vertex is located at the center of a catalyst particle. It contains information on the current particle radius and the local concentration of Pt-ion governed by the electrochemical model of Pt-dissolution and plating. The spherical surface of each particle is partitioned by a Voronoi tessellation, and each spherical-polygon mesh element is called satellite. All the satellites belonging to the same spherical shell are associated to one vertex. The satellites are the medium in which dissolved Pt (adjacent to a particle's surface) diffuse around a particle—each satellite communicates with its neighbors similar to surface diffusion. In addition, satellites can be thought of as a local particle atmosphere that communicates material to a particle via a Butler-Volmer current. The separation between vertex and satellites allows to treat separately transport and electrochemical reactions, and it provides a representation for the boundary-layer, i.e., a surface layer

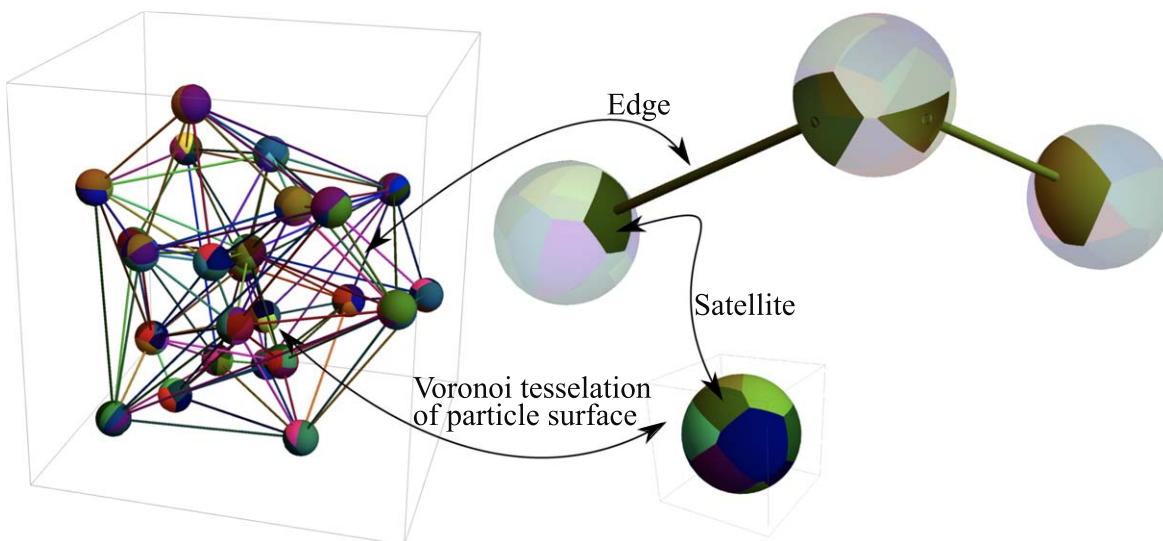


**Figure 2.** The mesoscale model for Ostwald ripening of platinum nanoparticles is illustrated. The satellites derive from a Voronoi tessellation of the particle surface. Surface diffusion is modeled through the exchange of flux between neighbouring satellites of a given particle. The electrochemical reactions are embedded at the vertices. The dissolution rate increases with decreasing particle size, and diffusion along edges allows for the re-distribution of mass through the network. Differences in concentration between satellites (on two different particles) connected by an edge, produce a flux that is inversely proportional to the edge length. (For a more clear representation, the left image contains only a subset of the particles shown in Fig. 1 and used to produce the results presented here).

characterized by local excess concentration of Pt-ions in solution. Each satellite contains information about its relative surface area, the relative distance to and border-length with neighbouring satellites. Additionally, a satellite has its own time-dependent concentration.

A packing model is used to generate a representative volume of the CCL microstructure (as illustrated in the left panel of Fig. 1) and determine the position of the Pt-particles over the carbon support. The microstructure in Fig. 1 consists of spherical Vulcan-type carbon particles with mean size of 30 nm, and coated by an ionomer layer of thickness 3–5 nm. The Pt-particles decorate the carbon support, and the Pt/C ratio was fixed at 0.2 weight ratio.

A 3D Delaunay triangulation having nodes located at the particles' center is used to construct the edges in the network model and represent the connectivity among neighbouring particles. The triangulation connects the particles' center with straight lines and does not take into account the curvature of the carbon support. This approximation can be removed in future implementations of the model. To account for ionomer poisoning of the catalyst, a scaling factor between the geometric surface area and the ECSA could be defined for each Pt-particle depending on its interaction with the ionomer.

Edges connect satellites belonging to different particles. All the edges and satellites together form a fully connected diffusion network that allows for the redistribution of mass of dissolved platinum. The complete list of information contained in the data-structure is listed in Table A-I of the Appendix.

**Diffusion and electrochemical model.**—Upon voltage cycling, electrochemical dissolution tend to release Pt-ions, allowing them to diffuse from one particle to another and even leave the cathode catalyst layer. The dissolved ions tend to deposit on larger particles, resulting in growth of large particles at the expense of smaller ones. Platinum mass loss and redistribution leads to loss in catalytic surface area available for the oxygen reduction reaction. The transport of platinum ions is mediated by the water generated from the electrochemical reaction at the cathode and from vapor condensation.

The model accounts for three mechanisms of Pt-ion transport with the definition of three fluxes: the flux  $J^{\text{ptct}}$  within the boundary layer, the flux  $J^{\text{sat}}$  over the particle surface, and  $J^{\text{dge}}$  along the edges connecting particle-pairs. The steady-state fluxes are in nanomoles per unit of time and their definitions are listed in Table I.

The flux Eqs. in Table I have the following general form

$$\begin{aligned} \text{flux}_{AB} &= \text{diffusivity} \times \text{concentration gradient} \times \text{cross-section} \\ &= \text{diffusivity} (nm^2/s) \left( \frac{\text{nanomoles}_B (nmol)}{\text{volume}_B (nm^3)} \right. \\ &\quad \left. - \frac{\text{nanomoles}_A (nmol)}{\text{volume}_A (nm^3)} \right) \frac{\text{section}_{AB} (nm^2)}{\text{distance}_{AB} (nm)} \end{aligned}$$

For instance the gradient along the edge is computed from the difference in concentration at the end satellites divided by the edge length. The gradient is multiplied by the cross-section of the edge, in turn expressed as a fraction of the satellite's surface area through  $S_{\text{link}}$ .

The expression of the flux through the boundary layer  $J^{\text{ptct}}$  derives from the product between the gradient across the boundary layer  $(n_{iv} - n_i)/\delta$  and the satellite surface  $S_p \pi r_i^2$ , divided by the volume of the spherical shell  $4\pi r_i^2 \delta$ .

In this version of the model, Pt-ions can diffuse within the network, and the total mass is conserved. The equilibrium condition for vertices

$$J_i^{\text{ptcl}} + J_i^{\text{diss}} = 0, \quad \forall i \in \text{ptcls} \quad [6]$$

is a balance between the dissolution flux and the flux through the boundary layer. The mass-conservation condition at the satellites

$$\sum_{i,j \in \text{all edges}} J_{i\alpha \rightarrow j\alpha}^{\text{edge}} + \sum_{i \in \text{ptcls}} \left( \sum_{\alpha \in \text{sat of } i} J_{i\alpha}^{\text{sat}} - J_i^{\text{ptcl}} \right) = 0 \quad [7]$$

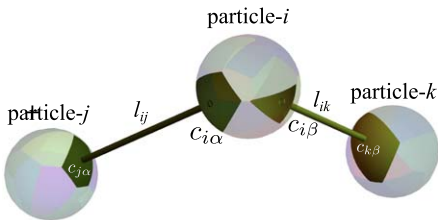
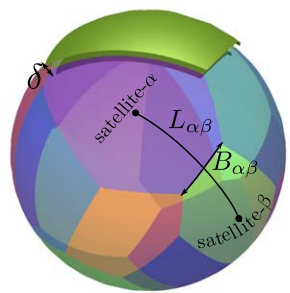
includes the contribution of the neighbouring satellites, the flux from the particle surface and the diffusion along the edge. A sink mechanism can be included to simulate Pt-mass loss due to reaction with hydrogen-gas cross-over.

The numerical implementation of the model was coded in the Wolfram Language and simulated using Mathematica.<sup>18</sup>

The main transport parameters are: the diffusivity  $D_{TL}$  of Pt-ion along the triple line (represented by the edge), the surface diffusivity  $D_S$ , and the diffusivity through the boundary layer  $D_{BL}$ . The vehicle for Pt-ion diffusion and mass redistribution is not well understood. The value for the edge diffusion  $D_{TL}$  is an empirical representation of the Pt-ion diffusivity within the CCL microstructure. It is not



Table I. Equations for electrochemical dissolution/plating of platinum and transport of dissolved platinum through the network.

Flux along edges	
$J_{i\alpha \rightarrow j\alpha}^{\text{edge}} = D_{TL} \frac{n_{j\alpha} - n_{i\alpha}}{l_{ij}} \frac{S_{\text{link}}}{\delta} \quad (1)$	
<ul style="list-style-type: none"> <li>• <math>i, j</math>: indices of the satellite pairs defining each edge</li> <li>• <math>D_{TL}</math> diffusivity along the edge (1000 nm<sup>2</sup>/s)</li> <li>• <math>(n_{j\alpha} - n_{i\alpha})/l_{ij}</math>: steady state gradient (nmol/nm)</li> <li>• <math>S_{\text{link}}</math>: cross-section area of the link relative to the satellite area (1)</li> <li>• <math>\delta</math>: boundary layer thickness (nm)</li> </ul>	
Flux over the particle's surface	
$J_{i\alpha}^{\text{sat}} = D_S \sum_{\nu \in \text{nbrs of } \alpha} \left( \frac{n_{i\alpha}}{S_\alpha} - \frac{n_{i\nu}}{S_\nu} \right) \frac{1}{r_i^2} \frac{B_{\alpha\nu}}{L_{\alpha\nu}} \quad (2)$	
<ul style="list-style-type: none"> <li>• <math>\alpha</math>: each satellite belonging to particle <math>i</math></li> <li>• <math>\nu \in \text{nbrs of } \alpha</math>: all satellites that abut satellite <math>\alpha</math> of particle <math>i</math></li> <li>• <math>D_S</math> surface diffusivity (1 nm<sup>2</sup>/s)</li> <li>• <math>S_\nu</math>: satellite <math>\nu</math> normalized surface area (<math>\sum_{\nu \in \text{satellites of } i} S_\nu = 4\pi</math>)</li> <li>• <math>B_{\alpha\nu}</math>: normalized border length between satellites <math>\alpha</math> and <math>\nu</math></li> </ul>	 <ul style="list-style-type: none"> <li>• <math>L_{\alpha\nu}</math>: normalized distance between the center of mass of satellite <math>\alpha</math> and <math>\nu</math></li> <li>• <math>r_i</math>: radius of particle <math>i</math> (nm)</li> </ul>
Flux through the boundary layer	Pt-dissolution flux
$J_i^{\text{ptcl}} = D_{BL} \sum_{\nu \in \text{satellites of } i} \frac{n_{i\nu} - n_i}{\delta^2} \frac{S_\nu}{4\pi} \quad (3)$	$J_i^{\text{diss}} = 4\pi r_i^2 k^{\text{diss}} \left( e^{\frac{2\alpha F}{RT}(V-U(r_i))} - \frac{c_i}{c_i^{\text{ref}}} e^{-\frac{2\alpha F}{RT}(V-U(r_i))} \right) \quad (4)$
<ul style="list-style-type: none"> <li>• <math>\nu</math>: each satellite belonging to particle <math>i</math></li> <li>• <math>D_{BL}</math> diffusivity through the boundary layer (10 nm<sup>2</sup>/s)</li> <li>• <math>n_i</math>: nanomoles at the particle surface (nmol)</li> <li>• <math>n_{i\nu}</math>: nanomoles at the satellite <math>\nu</math> of <math>i</math> (nmol)</li> <li>• <math>S_\nu</math>: satellite <math>\nu</math> normalized surface area</li> <li>• <math>\delta</math>: boundary layer thickness (1 nm)</li> </ul>	$U_{Pt}(r_i) = U_{Pt}^o - \frac{\gamma_{Pt}\Omega}{Fr_i}; \quad \frac{dr_i}{dt} = \frac{\Omega J_i^{\text{diss}}}{4\pi r_i^2} \quad (5)$ <ul style="list-style-type: none"> <li>• <math>U(r_i)</math>: dissolution potential for a particle <math>i</math> of radius <math>r_i</math> (V)</li> <li>• <math>k^{\text{diss}}</math>: dissolution kinetics (10<sup>-11</sup> mol / cm<sup>2</sup> · s)</li> <li>• <math>c_i = n_i/(4\pi r_i^2 \delta)</math>: concentration at the particle surface normalized by reference value <math>c_i^{\text{ref}} = 1</math> M</li> <li>• <math>\Omega</math>: partial molar volume (9.29 cm<sup>3</sup> / mol)</li> <li>• <math>\gamma_{Pt}</math>: surface energy (2.78 J / m<sup>2</sup>)</li> <li>• <math>\alpha</math>: anodic and cathodic charge transfer coefficient (0.5)</li> </ul>

know if the preferred diffusion pathway for Pt-ions is through liquid water or ionomer, or both. Therefore,  $D_{TL}$  may depend on all of the following properties

- diffusivity the Pt-ion in bulk water,
- liquid-water saturation of cathode catalyst layer (which in turn depends on the relative humidity and on the wetting property of the substrate),

- diffusivity the Pt-ion in Nafion as a function of its water saturation
- ionomer dispersion

The bulk diffusivity of Pt-ions in water may be in the order of 10<sup>-5</sup> cm<sup>2</sup> s<sup>-1</sup> according to the values estimated for other transition metals like Ni.<sup>19</sup> Atomic surface diffusion on Pt nanoparticles has been quantified by high-resolution transmission electron microscopy

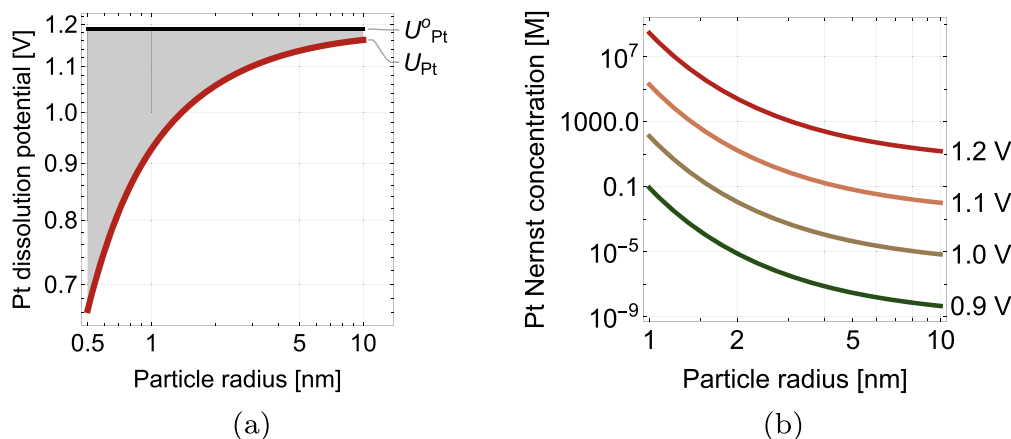


**Figure 3.** (a) The reference potential for platinum dissolution  $U_{Pt}^0 = 1.18$  is marked by a black line. This is the thermodynamic potential expected from Pourbaix's diagram<sup>21</sup> and it refers to a Pt thin-film (radius of curvature  $\rightarrow \infty$ ). For Pt-nanoparticles the dissolution potential depends on the particles radius as illustrated by the red curve. The potential  $U_{Pt}(r)$  is computed according to Eq. 5-a and the calculated surface energy  $\gamma_{Pt} = 2.78 \text{ J m}^{-2}$ . (b) The equilibrium concentration of Pt in solution is plotted according to the Nernst Eq. 12. Each curve correspond to a different voltage. A strong dependence on the particle size can be observed particularly for radii  $r_p < 2 \text{ nm}$ .

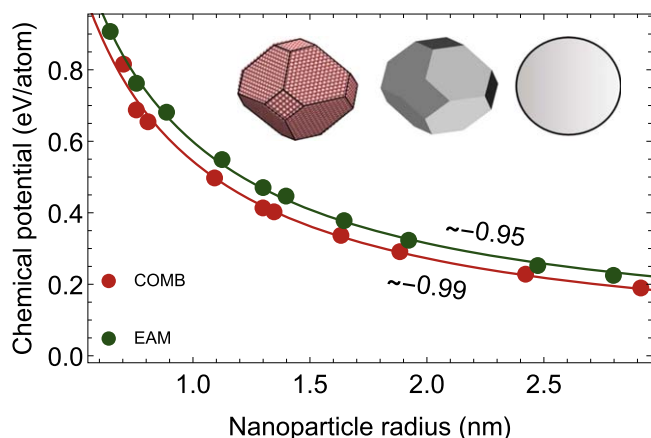


**Figure 4.** The change of chemical potential  $\Delta\mu_{atomistic}$  for different NP sizes using EAM and COMB force fields. Using power law fitting for simulated points demonstrated an  $r_{NP}^{-0.99}$  dependence for COMB and  $r_{NP}^{-0.95}$  for EAM, both in very good agreement with  $r_{NP}^{-1}$  derived from the Gibbs-Thomson relation. Using Eq. 8, the equivalent surface energy  $\gamma_{Pt}$  can be evaluated as written in Table II.

(TEM) in vacuum to be in the order of  $10^{-17} - 10^{-16} \text{ cm}^2 \text{ s}^{-1}$ .<sup>20</sup> It is yet to be determined whether Pt diffuse faster in Nafion and in what form. In the numerical analyses presented here, we assumed the following values for the diffusivity constants  $D_{TL} = 1000 \text{ nm}^2 \text{ s}^{-1}$ ,  $D_S = 1 \text{ nm}^2 \text{ s}^{-1}$ ,  $D_{TL} = 10 \text{ nm}^2 \text{ s}^{-1}$ , but these values will need to be adjusted as we learn more about the physics of Pt-mass redistribution.

The electrochemical adsorption/desorption of platinum is modeled by a Butler-Volmer equation (see Eq. 4 in Table I). In Eq. 4, the parameter  $k^{\text{diss}}$  represents the surface reaction kinetics, and  $U_{Pt}(r_p)$  is the particle-size dependent dissolution potential. The rate of change of the particle radius follows from the dissolution flux according to Eq. 5-b.

The dissolution flux grows exponentially with decreasing particle size. To prevent numerical instabilities the model includes a cut-off radius (here set to 0.5 nm). Once the particle size approaches the cut-off radius, the remaining mass of platinum is assumed to dissolve within the next time step. This simple approach prevents the dissolution flux to grow unbounded as the radius  $r_p \rightarrow 0$ .

The dissolution potential  $U_{Pt}$  diverges from its reference values  $U_{Pt}^0 = 1.18 \text{ V}$ <sup>21</sup> as the particle size decreases (see Fig. 3a). The

**Table II. Evaluated bulk and surface properties of Pt.**

Property	EAM	COMB
Lattice constant (Å)	3.91	3.9
Bulk energy (eV atom <sup>-1</sup> )	5.77	5.774
$\gamma_{(111)}$ (J m <sup>-2</sup> )	2.08	1.71
$\gamma_{(110)}$ (J m <sup>-2</sup> )	2.39	2.27
$\gamma_{(100)}$ (J m <sup>-2</sup> )	2.17	2.2
$\gamma_{Pt}$ (J m <sup>-2</sup> )	2.796	2.776

Gibbs-Thomson expression relates the particle radius to the chemical potential of its Pt crystallite. The bigger the particle, the smaller its chemical potential. The Gibbs Thomson relation reads

$$\Delta\mu = 2\Omega\gamma_{Pt}/r_p. \quad [8]$$

This expression assumes spherical Pt particles which is a simplification to the faceted structure of Pt nanoparticles (NPs). In fact, Pt has a face-centered-cubic structure (FCC) and the thermodynamic equilibrium shape of its NPs is governed by the surface energies of its high symmetry planes ( $\gamma_{(111)} < \gamma_{(100)} < \gamma_{(110)}$ ).<sup>22</sup> Hence, the equilibrium shape of Pt-NPs is a truncated octahedron and the NP surface is predominantly (111) faceted (see Fig. 4). While empirical evidence suggests that the Gibbs-Thomson effect applies to faceted NPs,<sup>15</sup> it is unclear what the range of validity of Eq. 8 is and what value of  $\gamma_{Pt}$  is to be used especially at the limit of small NP sizes. The increased chemical potential could be computed with the anisotropic analog of surface tension multiplied by curvature—the weighted-mean-curvature,<sup>23</sup> but it becomes increasingly challenging when we transition to nanoclusters.

We employ simple molecular mechanics energy minimization to evaluate the potential energies of different size crystalline Pt-NP at their equilibrium shape using the Wulff construction. Calculations were conducted using the large-scale atomic/molecular massively parallel simulation (LAMMPS) tool.<sup>24</sup> We use a commonly applied Embedded Atom Method (EAM) force field (Interatomic Potentials Repository—National Institute of Standards and Technology NIST)<sup>25</sup> and a recently developed reactive one; namely, Charge Optimized Many Body (COMB) potential<sup>26,27</sup> for comparison. Surface energies of the high symmetry facets were evaluated using the Fiorentini and Methfessel method<sup>28</sup> where  $U_{slab} = 2\gamma_{slab} + NU_{bulk}$ , in which N is the total number of atoms in the slab and  $\gamma_{slab}$  is the surface energy. By plotting the energy of a multi-layer slab vs N it is possible to derive  $2\gamma_{slab}$  as the

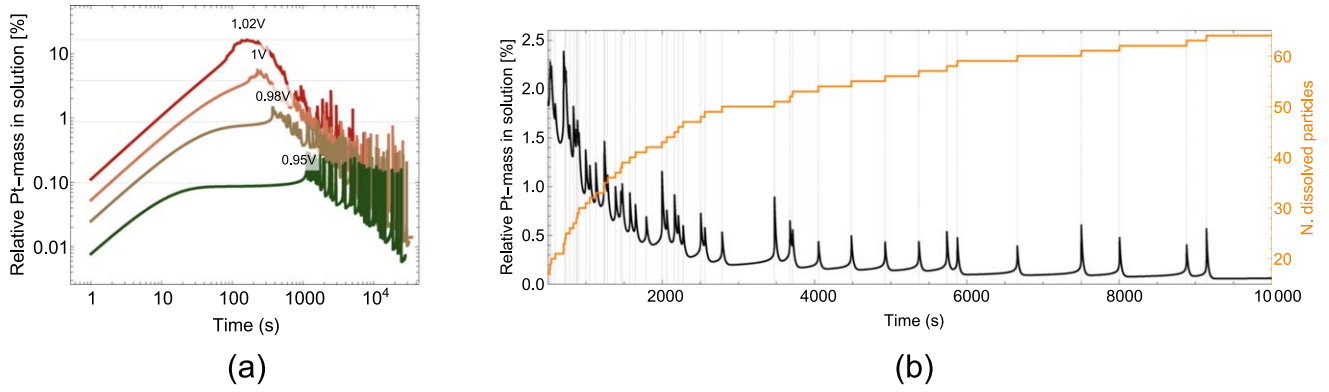


**Figure 5.** (a) The amount of platinum dissolved at a given time depends on the applied voltage and on the particle size distribution. For all the four cases illustrated here, the amount of Pt in solution increases over time, until it approaches the mean field concentration computed as  $\sum_i c^{eq}(V, r_i)/N$  (with  $N$  being the total number of particles at time zero) and marked by the horizontal grid lines. As the particles coarsen the amount of dissolved Pt decreases, following the relationship, in Eq. 12, between the equilibrium concentration of the dissolved species and the average particle radius. (b) The image shows in details the descending part of the curve from Fig. a for the case of a voltage hold at 1 V. The vertical gray lines highlight the correspondence between each dissolution peak (black curve) and the increment in the number of dissolved particles (orange curve).

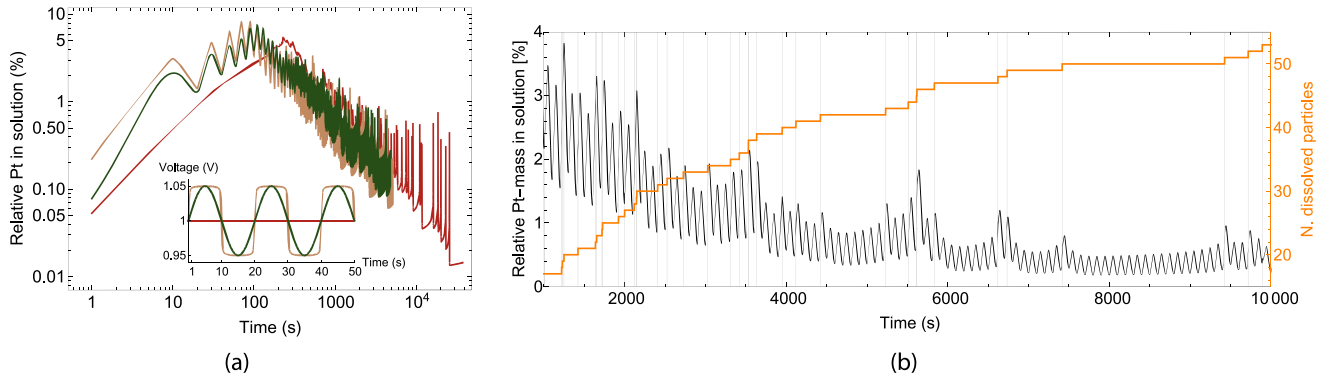


**Figure 6.** (a) The amount of dissolved platinum for two voltage cycling tests (with voltage ranging from 0.95 V to 1.05 V) is compared to the voltage hold experiment at 1 V. As shown in the figure inset, the voltage cycling curves are a triangle wave (green curve) and square wave (yellow curve), with frequency 1/20 s. (b) The dissolution peaks are shown by a black line. They include peaks that follow the frequency of the voltage cycling and additional peaks (marked by vertical gray lines) corresponding to an increase in the number of dissolved particles (orange step- function). In the time interval (6000–10000) s the distinction between the two type of dissolution peaks is more evident.

intersect and bulk energy  $U_{bulk}$  as the slope of the slab potential energy  $U_{slab}$  vs  $N$  curve.

A summary of the  $\gamma_{slab}$  for different planes and force fields is provided in Table II. Both force fields estimate similar  $U_{bulk}$  and lattice constant. In addition, the ranking of  $\gamma_{slab}$  values for different facets was as expected for high symmetry planes, with  $\gamma_{(111)}$  having the lowest magnitude. However, different  $\gamma_{slab}$  ratios would result in a slightly different equilibrium NP shapes.

We define the chemical potential of the Pt atoms extracted from atomistic simulations as follows

$$\Delta\mu_{atomistic} = \frac{U_{NP}}{N} - U_{bulk} \quad [9]$$

where  $U_{NP}$  is the potential energy of the NP. Here,  $\Delta\mu_{atomistic}$  should be inversely proportional to the particle radius, as suggested by the Gibbs-Thomson relation, but the definition of a spherical radius is ambiguous for a faceted NP. One approach to address that is to employ the quantity  $R_g$  (radius of gyration) to evaluate an equivalent spherical radius.<sup>29,30</sup> The  $R_g$  can be evaluated as:

$$R_g = \sqrt{\frac{1}{N} \sum_i |R_i - R_{cm}|^2} \quad [10]$$

In Eq. 10,  $R_i$  denotes the coordinate of the  $i$ th atom of the nanoparticle and  $R_{cm}$  is the coordinate of the NP center of mass.

We propose employing a modified equivalent spherical radius of the NP that is calculated according to

$$r_{NP} = R_g \sqrt{5/3} - r_{Pt-atom} \quad [11]$$

with  $r_{Pt-atom}$  being the radius of the Pt atom. The shift using  $r_{Pt-atom}$  resulted in a good match with the continuum theory as discussed below.

In Fig. 4, the plot of  $\Delta\mu_{atomistic}$  vs  $r_{NP}$  shows a smoothly decreasing function that can be fit by a power law. The COMB potential results in power of  $-0.99$  while EAM data decays with a power of  $-0.95$ , both in very good agreement with the Gibbs-Thompson exponent of  $-1$ . The results in Fig. 4 show that the Gibbs-Thompson relation can be extended to faceted nanoparticles by defining an equivalent spherical particle which is derived from the radius of gyration (please refer to Appendix for direct energy evaluation of NP of varying sizes). We believe that the  $r_{Pt-atom}$  shift is originated from the nonlinear relation between the number of atoms along different directions and their interaction energies especially in small atomic clusters.<sup>31</sup> Hence, a small shift on the order of atomic radius, Gibbs-Distance,<sup>31,32</sup> would be needed to achieve the proper transition from the atomistic to the continuum model. In addition, a single intrinsic value of free energy  $\gamma_{Pt}$  can be employed to describe the state of NPs in continuum models. The extracted value of  $\gamma_{Pt}$  is considered as a weighted mean surface energy.



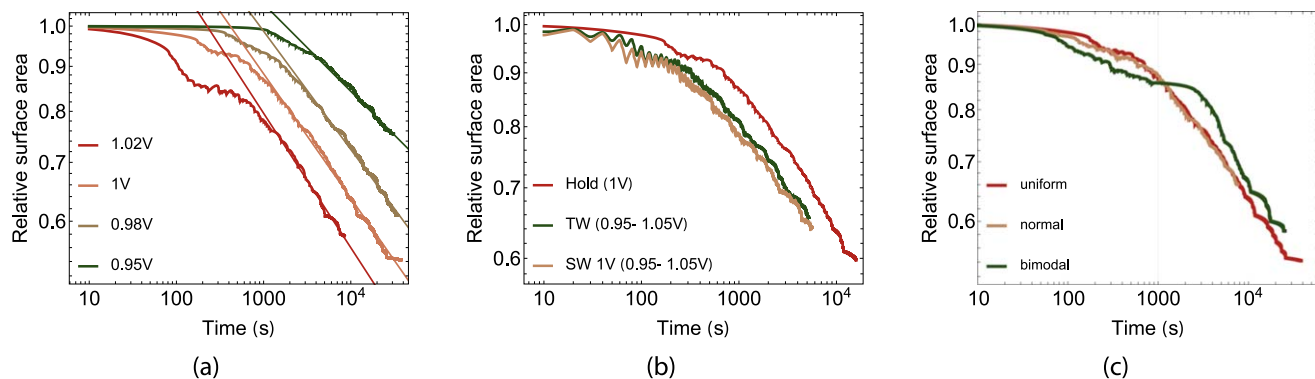


**Figure 7.** (a) Surface area loss vs time is plotted for the four voltage-hold simulations in a logarithmic scale. Each 20–30 mV voltage shift causes a significant difference in the rate of particle coarsening and in the loss of active surface area. The time scaling extracted from the slope of the curves is  $\sim t^{0.15}$ ,  $\sim t^{0.14}$ ,  $\sim t^{0.13}$ ,  $\sim t^{0.1}$  in decreasing order of voltage. (b) The surface area loss from two voltage cycling experiments is compared to the case where voltage is held constant at the mean value. The red curve represents the constant-voltage test already shown in (a) and it is used as a reference for the curves relative to the triangular wave (green curve) or a square wave test (yellow curve). The three surface area vs time curves have the same slope, but cycling the voltage (between 0.95 and 1.05 V) tends to accelerate coarsening. (c) The evolution of three particle size distributions under the same voltage conditions is analyzed. The uniform and normal PRD tend to converge after 1000 s, while the bimodal PRD has the most distinct coarsening: initially it suffers from a larger surface loss, but the coarsening significantly slows down once the smaller particles are dissolved.

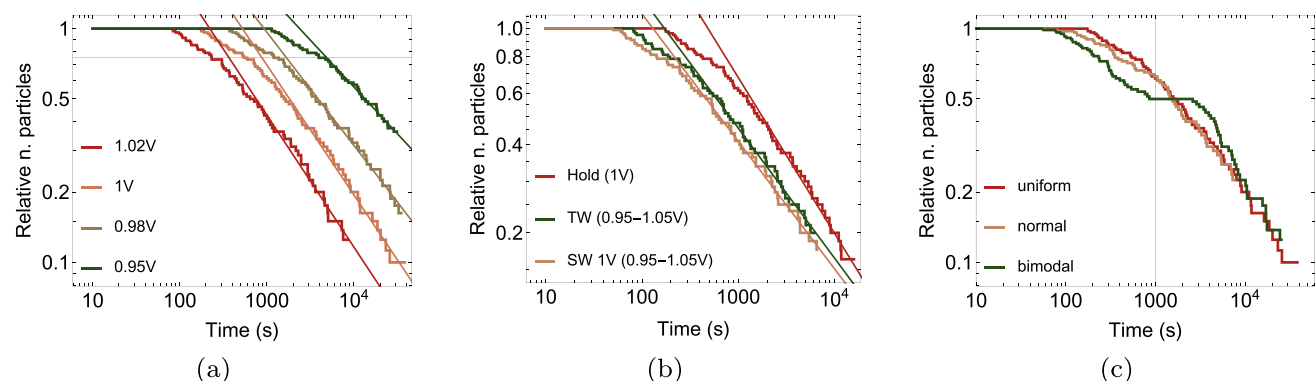


**Figure 8.** (a) The time scale for the evolution of the number of particles shows a dependence on the applied voltage. (b) Similarly to Fig. 7b, the same slope characterizes the curves for different voltage cycling conditions. This means that the time scaling is the same, however more particles dissolve when the voltage oscillates around the mean value of 1 V. (c) The effect of particle size distribution is only visible in the first 1000 s for the normal and uniform PRD (yellow and red curve). The bimodal PRD may converge to the same curve but on a time scale that is one order of magnitude larger.

It is noted that despite the difference in surface energies in EAM and COMB force fields and hence the slight difference in the NP Wulff shape, the magnitude of  $\gamma_{Pt}$  only differs by 0.7% (see Table II). Such small difference might stem from the homogenizing effect of transforming a faceted NP into a sphere which minimizes the intricate differences in the particle shape. The value of  $\gamma_{Pt}$  is high compared to the  $\gamma_{slab}$  of the high symmetry planes. This could be attributed to the rough surface of the reconstructed equivalent sphere for an FCC atomic structure with predominantly under-coordinated atoms at the surface.<sup>33</sup>

Rigorous evaluation of the faceted NP surface energy can, in principal, be attained using the weighted mean curvature;<sup>23</sup> however, our approach provides a simple and efficient estimate of the NP surface energy.

For a given voltage  $V$ , the equilibrium concentration of Pt in solution varies locally as a function of the particles size. The equilibrium concentration around each particle of radius  $r_p$  can be computed by the Nernst equation as follows

$$c^{eq}(V, r_p) = \text{Exp} \left[ 2 \frac{V - U_{Pt}(r_p)}{RT/F} \right] \quad [12]$$

The dependency of the Nernst concentration on the particle size is illustrated in Fig. 3b. For a given voltage in the range of 0.9 – 1.2 V, the value of  $c^{eq}(V, r_p)$  spans over several orders of

magnitude as a function of the particle size. (In Fig. 3b, we assumed a typical PEM fuel cell operating temperature of 80 °C.)

When the voltage is held above the dissolution potential, each particle dissolves until the local concentration of Pt in solution reaches the equilibrium value. A perfectly uniform particle size distribution represents a metastable state: it leads to uniform Pt-ion concentration and no mass diffusion within the system. However, any small perturbation in particle size, and hence local concentration, can initiate coarsening. The amplitude of the perturbation grows over time at a rate that is limited by mass transport and surface kinetics. Local fluxes tend to accumulate Pt-ions around the largest particles, thereby causing supersaturation of the solution around the particle surface and electroplating.

In the limit of zero Pt-volume fraction, the LSW equation for the kinetics of coarsening in the diffusion-limited regime is

$$K_{LSW}^D = \frac{8D\gamma_{Pt}\Omega^2 c^{eq}(V, \infty)}{9RT} \quad [13]$$

with  $K_{LSW}^D$  being the prefactor in the power law for the average radius  $\langle r \rangle^3 = \langle r_0 \rangle^3 + K_{LSW}^D t$ , and  $c^{eq}(V, \infty)$  the equilibrium concentration of platinum in solution for a perfectly flat solid/liquid interface. In the microstructural case, the Pt-diffusivity  $D$  includes a tortuosity factor due to the network of transport pathways, and it represents an empirical average of the three diffusion mechanisms embedded in the network model.

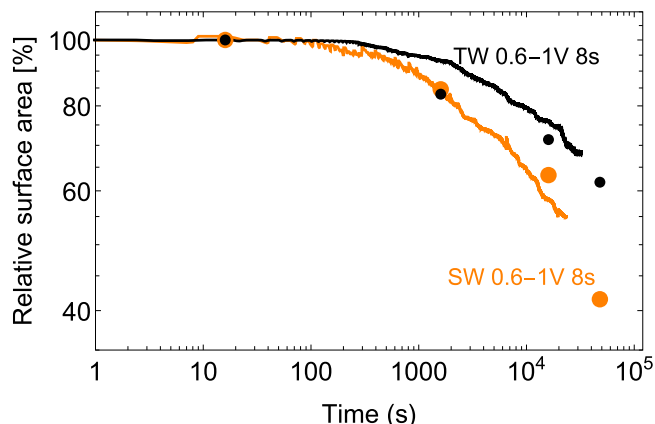


**Figure 9.** The relative ECSA measured during accelerated stress tests by Harzer et al.<sup>37</sup> is shown in comparison with predicted values by the Ostwald ripening model. The experimental data is marked by points and the simulation data is marked by curves. The prediction is fairly accurate for both triangular-wave (shown in black) and square-wave tests (in orange) between 0.6 and 1 V with 8 s half-cycle

Following the strong dependence of the equilibrium concentration on the the applied voltage, the LSW kinetic coefficient will also be sensitivity to the voltage. In the next section, the coarsening kinetics extracted from the simulations is compared to the scaling predicted by the LSW theory. Equation 4 and Eq. 5 are similar to the Darling and Meyers model,<sup>34</sup> but a factor of 2 was applied to Eq. 6 of Ref. 34 for consistency with the Gibbs-Thompson Eq. 8. In this implementation we did not consider the effect of the oxide coverage. A variety of approaches have followed the initial interpretation of Darling and Meyers as purely passivating layer.<sup>35</sup> Recent electrochemical models<sup>35,36</sup> employed a non-ideal solid solution theory to describe the observed coupling between the equilibrium dissolved Pt concentration and potential. Activity coefficients of Pt and  $\text{PtO}_x$  were correlated to oxide coverage. In general, electrochemical models for Pt-dissolution with different levels of details can be hosted by the vertices of this data-structure.

The effect of carbon corrosion can be included by modeling its affect on the position and interactions of Pt-nanoparticles. In terms of modeling, carbon corrosion may alter the inter-particle distance, cause mass-loss due to particle detachment, and may require significant re-meshing of the network during the simulation. Migration of Pt-nanoparticles over the substrate can be described

as a thermal fluctuation of the particle location, leading to a random walk over the curved carbon surface.

By decreasing the distance between particles, both carbon corrosion and particles migration may increase the probability of agglomeration and coalescence. A simple approach to modeling particle collision includes fixing a minimum distance between particles. Once such distance is reached, the entire mass of the smaller particle is transferred to the larger one (in one time step or gradually as a result of mass transport along the edge bridging the particles).

## Results

We performed numerical experiments with an ensemble of 80 particles dispersed in a volume of 100 nm in each spatial dimension. A packing model was used to generate a cluster of primary carbon particles of 30 nm average size, and coated by a ionomer layer of thickness 3–5 nm. From the microstructure shown in the left image of Fig. 1, a subset of Pt-particles was extracted to form the network structure illustrated in center image of Fig. 1. The average inter-particle distance, from Pt-particle center to Pt-particle center, is 35 nm. The linear distance is a simplification to the curved path taken by the Pt-atoms due to carbon particle curvature. Unless noted otherwise, the Pt-particle radius distribution is uniform in the range of 0.8–2.0 nm.

First, voltage-hold tests were performed to analyze the kinetics of particle coarsening as a function of the voltage. In the simulation, the evolution in each particle radius and the local concentration of platinum in solution were tracked. Figure 5a illustrates the relative amount of dissolved platinum (as nanomoles of Pt in solution normalized by the total nanomoles of platinum available in the system). Each curve in Fig. 5a shows a similar trend. The concentration of Pt in solution increases until the mean-field concentration for each applied voltage is reached asymptotically. The mean field concentration is computed as the average of the equilibrium concentration around each particle  $i$  as  $\sum_i c^{eq}(V, r_i)/N$ , with  $N$  being the total number of particles at time zero. Coarsening begins as the peak mean concentration is reached. The completed dissolution of a particle causes sudden increase of Pt concentration in solution, this is represented by the spikes in the descending part of the curves in Fig. 5a. This is clearly illustrates in Fig. 5b, with the overlay of the plot of the number of dissolved particles vs time. The gray vertical lines show a perfect correspondence between an increment in the number of dissolved particles (orange line) and the concentration peaks (black line). The exponential decays

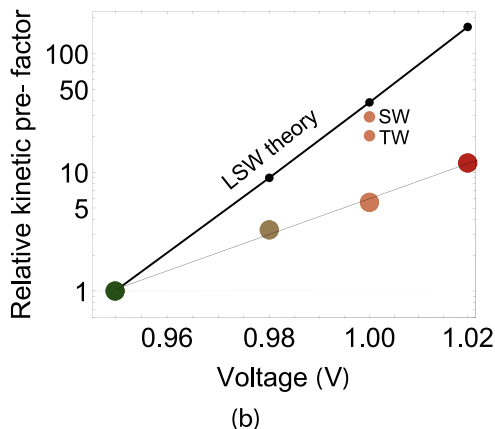
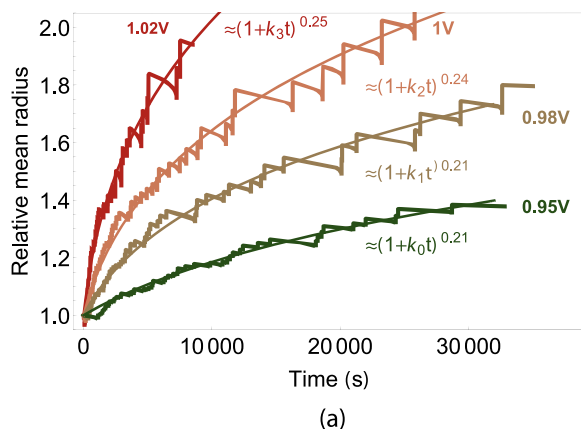


**Figure 10.** (a) The mean particle radius resulting from the coarsening simulations is plotted as a function of time on a linear scale. All the tests are performed at the constant voltage indicated on the curve. A power law of the form  $(1 + k_i t)^{p_i}$  was fitted to the numerical data, with the index  $i$  ranging from 0 for the lowest voltage (0.95V) to 3 for the highest voltage (1.02 V). The exponent  $p_i$  increases with the voltage from 0.21 to 0.24, but it remains lower than the time scaling expected from LSW theory. This may be attributed to the lower dimensionality of the diffusion through the network of edges, or in other words to the tortuosity of the diffusive pattern. (b) The coefficients  $k_i$  from the power law fitting in (a) are plotted normalized by the lowest value  $k_0$ . The black line represents the scaling in the kinetic coefficient expected from the LSW theory. The values are normalized with respect to the value computed at 0.95 V. The kinetic pre-factors computed for the TW and SW cycling are marked by pink points above the baseline value for the 1 V hold test.

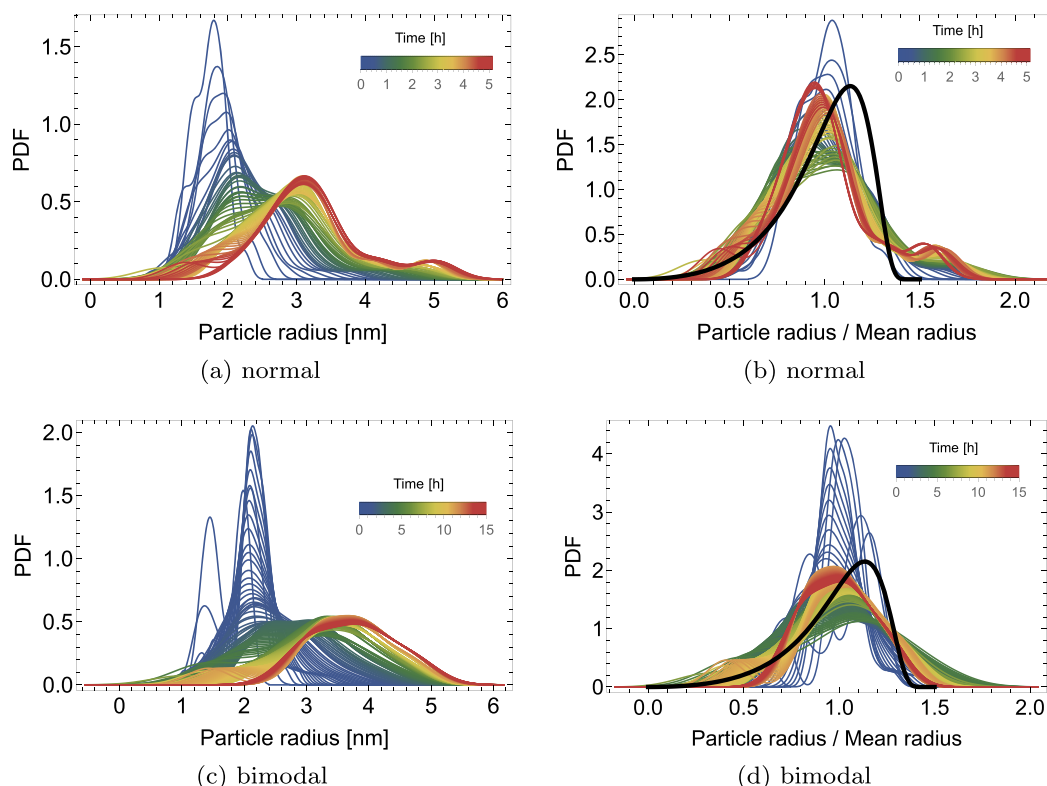


**Figure 11.** (a) Evolution of the particle radius distribution from an initial normal distribution with mean 1.75 nm and standard deviation 0.25 nm. The time-evolution is marked by the color of the curves, from blue ( $t = 0$ ) to red according to the legend. (b) PRD normalized with respect to the mean radius ( $r/\langle r \rangle$ ) is shown for the case of initial normal distribution. The black curve represents the steady-state LSW curve defined in Eq. 14. (c) Evolution of the PRD from an initial bimodal distribution generated from two normal distributions centered at 1.45 and 2 nm and both with 0.1 standard deviation. The lower peak tends to disappear in the 1000 s of the simulation. (d) Normalized PRD for the case of initial bimodal distribution is shown in comparison with the steady-state LSW curve marked in black.

following the spikes are controlled by mass transport and indicate the approaching of a new mean equilibrium concentration. On average the mean field concentration decreases during coarsening, as the average particle radius increases.

To study the effect of voltage cycling, initially two voltage cycling tests (with voltage ranging from 0.95 V to 1.05 V) were performed and the results compared with the voltage-hold experiment at 1 V. In the inset to Fig. 6a, the triangular wave (TW) and square wave (SW) tests are illustrated. In both cases, the voltage oscillates around the mean value of 1 V, with a frequency of 20 s for the full cycle. Figure 6a shows the amount of dissolved platinum with the peak concentration shifted earlier in time for the TW and SW cycling tests. Figure 6b shows the details of the descending part of the dissolution curve for the triangular wave case. The orange curve in Fig. 6b is a staircase function that shows the number of dissolved particles over time. Each step is marked by a vertical gray line to show the correspondence with some of the dissolution peaks. The remaining peaks are caused by the voltage cycling and are characterized by uniform frequency.

The trend in the surface area loss is investigated with respect to several factors. In Fig. 7a, the four voltage hold experiments clearly indicate that even a 20 mV shift in voltage causes a significant change in the coarsening rate. The kinetics and time scale of coarsening are both voltage-dependent, as indicated by the slope and intercept of the four curves in the logarithm-scale plot. A similar trend can be observed also in Fig. 8a, where the relative number of particles is plotted as a function of time. The system simulated here contains 80 particles at beginning of the simulation and in the most aggressive conditions, only 10–15 particles are left after 3 hours.

The effect of voltage cycling on the loss of active surface area and on the particle dissolution is illustrated in Figs. 7b and 8b

respectively. It is interesting to note that in both cases the slope of the curves for the TW and SW results follows approximately the same time scaling (same slope) as the constant voltage experiment at 1 V. The green (TW) and yellow curve (SW), are shifted with respect to the red curve, representing the baseline case of 1 V hold. The coarsening kinetics are accelerated by the voltage cycling, in particular in the case of square wave cycling, leading to more rapid aging. This example indicates how the proposed model can be used to predict aging under realistic driving cycle conditions, given that any functional form can be used to prescribe the voltage as function of time. In a future study we will explore the effects of the amplitude and frequency of the voltage wave on the coarsening kinetics and ECSA loss.

Two additional tests were performed to show the predictive capability of the model with respect to accelerated stress tests (ASTs). Triangular-wave (TW) and square-wave (SW) tests between 0.6 and 1 V with 8 s half-cycle are typical ASTs used to probe the durability of the cathode catalyst layer. The experimental data is extracted from Fig. 5 of Harzer et al.<sup>37</sup> for the samples with 0.4 mg<sub>Pt</sub>/cm<sup>2</sup>. Figure 9 shows a comparison between the measured relative ECSA loss (marked by points) and the predicted values (marked by curves).

We did not perform an extensive parametrization of the model, we simply used the same parameters as in the previous examples and only tuned the dissolution kinetics in Eq. (4) (increasing it by 5-fold) to improve the fit. We also employed the same particles spacing used in the previous analyses (in the experiments a Vulcan-carbon support was used). To approximately reproduce the PSD shown in the inset of Fig. 5 in Harzer et al.,<sup>37</sup> we assumed a normal particle size distribution with a mean radius of 1.5 nm standard deviation of 0.25 nm. Figure 9 shows that the model is able to capture the relative

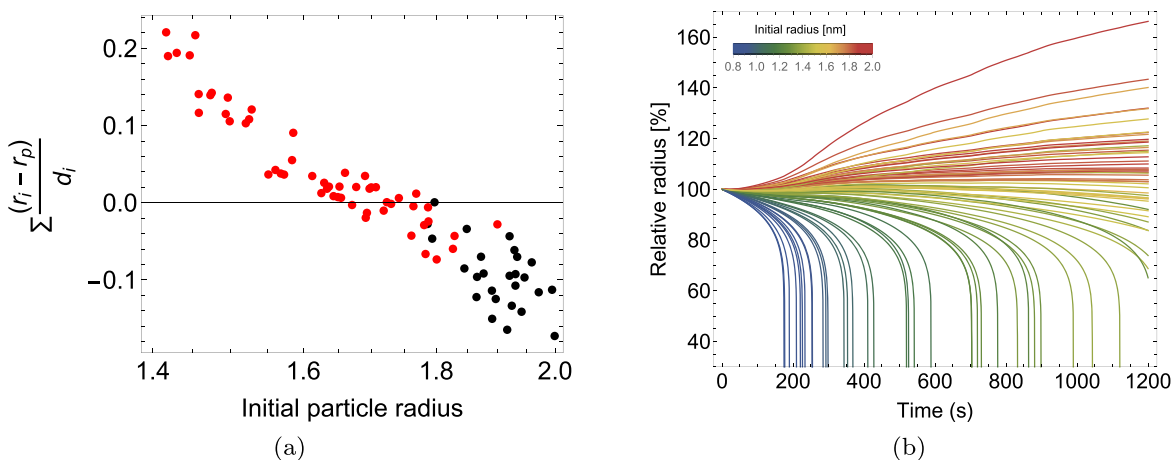


**Figure 12.** (a) For each particle, the function  $f_{sd}$  is the distance weighted average of the relative size of the neighbouring particles. The red points indicate particles that have a tendency to shrink and eventually dissolve. The black points identify particles that are coarsening. The points segregate around  $f_{sd} = 0$  which shows that the function is a good indicator of the coarsening behaviour. (b) The size evolution of each particles is tracked at the beginning of coarsening and is illustrated in relation to the initial radius (represented by the line's color). Blue lines correspond to smaller particles with radius close to 0.8 nm, and red particles have radii close to 2 nm. The mixing of green yellow and red curves indicates that the initial particle size is not the only contributing factor.

trend in surface area loss for both the TW (shown in black) and SW tests (in orange) in the first 10000 and 3000 cycles respectively. The simulation was interrupted when 90% of the initial particles were dissolved.

Further analyses were carried out on the effect of particle radius distribution (PRD). In addition to the baseline case with particle radius uniformly distributed in the range of 0.8–2.0 nm, two additional tests were performed at a fixed voltage of 1 V. First, a normal distribution with mean radius of 1.75 nm and standard deviation of 0.25 nm; second, a bimodal distribution centered around 1.45 nm and 2 nm. The particle locations and the initial total surface area were the same in each simulation. Figure 7c shows that the surface area loss for the normal PRD (yellow curve) converges to the one for the uniform PRD (red curve) after the first 1000 s. A similar trend is observed for the time evolution of the number of Pt nanoparticles (see Fig. 8c). We expect that the time to reach this steady state condition, where the coarsening is not sensitive to the initial PRD, increases with decreasing voltage and it also depends on the particular PRD. The bimodal distribution, consisting of a set of smaller particles and a set of larger ones, shows a different trend. The smaller particles tend to dissolve more rapidly, leading to a more extensive surface area loss before 1000 s (see green curve in Fig. 7c). Following this initial accelerated coarsening, there is a stalling period, where the surface evolves slightly and the number of particles stays constant.

The simulations were ended when the relative number of particles approaches 0.1 (i.e., 10% of the initial distribution), and at this point the three simulations have converged to approximately the same number of particles and relative surface area, independently of the initial PRD. The time scale for ripening to converge to the same trend depends on the specific operating conditions and model parameters.

The analysis of the average mean radius as function of time provides a comparison with the limiting regimes predicted by the LSW theory. A power law of the form  $(1 + kt)^p$  is used to fit the relative mean radius  $\langle r \rangle / \langle r_0 \rangle$  vs time  $t$  data, with  $\langle r_0 \rangle$  being the mean radius at time 0. The data extracted from the coarsening simulations and the power-law fit are plotted in Fig. 10a. In the case of coarsening limited by inter-particle diffusion, the LSW theory predicts  $p = 1/3$ . Conversely, when surface kinetics is the rate limiting phenomenon the exponent is expected to be  $p = 1/2$ . With the assumption of dissolution kinetics  $k^{diss} = 10^{-11}$  mol/cm<sup>2</sup>·s, and triple-line diffusion  $D_{TL} = 10^3$  nm<sup>2</sup>/s, the model's data produces

best-fit values of the exponent in the range  $0.21 \leq p \leq 0.25$ . The value of  $p$  scales linearly with the voltage. This may be interpreted as the relative contribution of dissolution kinetics and mass transport to be dependent on the applied voltage. However, this hypothesis needs to be investigated further with a larger ensemble of particles. Also the sensitivity on the parameters ( $k^{diss}$ ,  $D_{TL}$ ) should be considered in future studies.

Here we analyze the scaling of the coefficient  $k_i$  in the power-law fitting  $(1 + k_i t)^p$ , with  $i = 0, \dots, 3$  for the four voltage-hold experiments. In Fig. 10b, the black line represents the value of  $K_{LSW}^D(V)$  computed according to Eq. 13, normalized with respect of  $K_{LSW}^D(0.95V)$ . This provides the scaling with respect to the applied voltage, without taking into account the coefficients in Eq. 13, as those depend on the regime of coarsening, and on the parameters ( $k^{diss}$ ,  $D_{TL}$ ). Similarly, the four large points in Fig. 10b represent the values  $k_i/k_0$ , with  $i = 0, \dots, 3$  extracted from the power law fits shown in Fig. 10a. The scaling with respect to the voltage predicted by our model is one half of the one predicted by the LSW theory.

The assumptions of LSW may apply if the edge diffusivity and inter-satellite diffusivity are large compared to the Butler-Volmer current. In this case, each particle is more likely to be exchanging mass with the mean field produced by all of the particles. However, because of inter-particle diffusion (i.e., restricted to the region between carbon particles) is reduced, subsequent analysis may show that the power-law exponents are affected by the diffusion's reduced dimensionality.

On the other hand, if edge diffusivity is slow, each particle is interacting primarily with its proximate neighborhood: LSW would not apply. If the inter-satellite diffusivity and Butler-Volmer kinetics are slow, the proximity effect would be exacerbated. A particle would not be interacting with the average characteristics of its average neighborhood—it would be interacting with the extreme values of the radii of its neighborhood.

The coarsening kinetics for the voltage cycling tests is also marked in Fig. 10b to highlight the increase in coarsening rate (a factor of 3.49 and 5.6 respectively for TW and SW) with respect to the constant voltage test. However, the power law exponent for the square wave test is 0.17 and for the triangular wave is 0.18, both lower than the exponents 0.24 obtained for the voltage-hold tests (see Fig. 10a).

The evolution of the particle radius distribution over time is shown in the Fig. 11 for the cases with an initial normal PRD



(images a, b) and bimodal PRD (images c, d). The time flow is represented by the color of the curve, going from blue ( $t = 0$ ) to red. According to the LSW theory, a steady state normalized distribution function is approached asymptotically. For diffusion-limited coarsening, the steady-state normalized curve has the following equation (with  $\rho = r/\langle r \rangle$ , and  $h_0 = 0.014419$ )<sup>38</sup>

$$h(\rho) = \frac{1}{h_0} \frac{\rho^2}{\left(\frac{3}{2} - \rho\right)^{11/3} (\rho + 3)^{7/3}} \exp\left(\frac{3}{2\rho - 3}\right) \quad [14]$$

and it is plotted in black in images b and d of Fig. 11

The cases illustrated in Fig. 11 exemplify a trend that we observe also in the other examples that we analyzed, namely the normalized PRD tends to converge to a steady state curve that is similar to the LSW one but with the peak shifted to the left of  $\rho = 1$ . Also, a few particles larger than the cut-off value of  $1.5\langle r \rangle$  are observed. Further investigation is needed to understand if a unique steady-state PRD can be defined for this system as a function of the relative contribution of the dissolution and transport kinetics, and what is the time-scale for convergence.

Under the assumption that the total volume is conserved, an approximate relationship can be derived between the number of particles and the average radius as they evolve upon coarsening. If the particle radius distribution at time  $t$  has converged to the LSW steady-state function (Eq. 14), the following relationship holds

$$E[r^3(t)] = (E[r(t)])^3 \quad [15]$$

between the expectation value for the radius and its third power. In other words  $\langle r^3(t) \rangle = \langle r(t) \rangle^3$ . It follows that the total volume of Pt-nanoparticles can be expressed as a function of the mean radius and the number of particles

$$V_{NP}(t) = \sum_{i=1}^{N(t)} \frac{4}{3} \pi r_i^3(t) = N(t) \frac{4}{3} \pi \langle r(t) \rangle^3 \quad [16]$$

$$V_{NP}(t=0) = \sum_{i=1}^{N_0} \frac{4}{3} \pi r_{0i}^3 = N_0 \frac{4}{3} \pi \langle r_0 \rangle^3 \quad [17]$$

Here  $N(t)$ ,  $N_0$  are the number of particles at a generic time  $t$  and at time  $t = 0$  respectively;  $r_i(t)$  is the radius of particle  $i = 1, \dots, N(t)$  at time  $t$  and  $r_{0i}$  is the radius of particle  $i = 1, \dots, N_0$  at  $t = 0$ .

If we account for the mass of dissolved platinum at time  $t$ , and if not mechanism of Pt-mass loss is considered the total volume of Pt-nanoparticles is conserved. This leads to a scaling law between the evolution of the relative number of catalyst nano-particle and the average radius. Under the assumption that the relative average radius follows a power law scaling with exponent  $p$ , the number of particles scaling is

$$\frac{N(t)}{N_0} \sim \left( \frac{\langle r_0 \rangle}{\langle r(t) \rangle} \right)^3 \sim (1 + kt)^{-3p} \quad [18]$$

In the case of a normal PRD, Eq. 15 is replaced by the following

$$\frac{E[r^3(t)]}{(E[r(t)])^3} = 1 + 3 \left( \frac{\sigma}{\mu} \right)^2 \quad [19]$$

with  $\mu$  being the mean and  $\sigma$  the standard deviation of the PRD. For small values of  $\sigma$ , Eq. 16 can still be considered a good approximation. Numerical analyses show that Eq. 18 is approximately satisfied with the exponent in the range between  $-3p$  and  $-2.5p$ .

There are several ways to analyze the effect of the local environment on the competitive coarsening process. For instance, the correlation function  $f_{sd}$  illustrated in Fig. 12a is a distance

weighted average of the relative size of the neighbouring particles. If all the particles sharing an edge with a given particle are larger in size than the particle itself than  $f_{sd}$  takes a positive value. Conversely, if a particle is surrounded by smaller particles, the value of  $f_{sd}$  for that particle will be negative. In Fig. 12a, the vertical axis shows the value of the spatial correlation function at the beginning of coarsening and the horizontal axis represents the initial radius. The clear segregation of red points (indicating particles that are decreasing in size) and black points (for growing particles) in the positive and negative regions of the plot suggests that the function  $f_{sd}$  is a good indicator for the system behaviour. Figure 12a is representative of all the constant-voltage simulations with uniform particle size distribution. The function  $f_{sd}$  appears also to have some correlation to the particle size, but this is dependent on the model parameters (i.e., Pt-diffusivity, kinetics of dissolution and surface energy). Figure 12b shows, for each of the 80 particles, the evolution of its radius over time with applied voltage of 1 V. The rainbow coloring scheme of the curves illustrates the relationship between the initial particle size at the coarsening behaviour. While it appears that the smallest particles tend to dissolve first (blue curves) and the largest particles to grow, the trend for the intermediate cases is less clear and it depends on the local environment.

## Conclusions

The results extracted from the simulations are not in accord with predictions from mean-field coarsening-theories. Fitting the mean radius to  $\langle \dot{r} \rangle = (1 + kt)^p$  produces values  $p$  from  $0.21 \rightarrow 0.25$  that scale linearly as the voltage varies from  $0.95 \rightarrow 1.02$ . The mean-field LSW theories would produce exponents of  $\frac{1}{2}$  for interface-limited kinetics and  $\frac{1}{3}$  for diffusion-limited kinetics. Furthermore, the mean-field exponent would not depend on voltage.

It is possible that the limited number particles in the simulation is not sufficient to obtain good statistics. This requires further study. It is also possible that the selected diffusivities do not fall in either of the two limiting cases of LSW. However, if this is the case, then  $p$  (which is  $\approx \frac{1}{5}$ ) should be between  $\frac{1}{3}$  and  $\frac{1}{2}$ .

It is also possible that the reduced dimensionality of diffusion in our microstructural model does not conform to the LSW model. If this is the case, then we conclude that LSW should not be applied to coarsening in composite microstructures in which diffusivity is small in one of the phases—a microstructural model such as ours is necessary. We expect that trends like power-laws could be obtained by repeated Monte Carlo experiments with our method.

The presented model is attractive because it divides the simulation method into two parts. The first part is the data structure (particles, satellites, edges) that depend on connectivity and morphological features of the microstructures. The second part is the physics of dissolution and diffusion that is embedded into the data structure.

Numerical tests performed on a representative particle ensemble indicate a strong sensitivity of the coarsening rate on the applied voltage and on the surface tension.

Processes that alter the surface tension or creates a diffusion barrier on the particle surface would reduce coarsening, however they may also affect catalytic efficiency. For instance, high relative humidity is generally favorable for the performance of PEMFC, however it tends to increase the water saturation of of cathode catalyst layer, allowing for higher Pt-ion mobility and Pt-mass redistribution. Surface treatments that increase cathode hydrophobicity could compensate for water condensation and would be beneficial for durability.

A combination of experiments and modeling is required characterize the structural changes in platinum-based catalyst particles, and distinguish between several catalyst deactivation mechanisms



and transport pathways. Specialized liquid cell TEM techniques can provide direct imaging of motion and volume changes in individual catalyst nanoparticles during electrochemical cycling under realistic operating conditions.<sup>39</sup> Measurements of nanoparticle dissolution *in operando* with high spatial and temporal resolution would provide the data necessary for accurate parametrization of this model.

## Appendix

### Data-structure for the Network Model of Ostwald ripening

**Limitations of direct surface energy calculation for nanoparticles.**—A plot of a directly calculated NP surface energy  $\gamma$  for different NP sizes demonstrates the coupling between  $r_{NP}$  and the corresponding  $\gamma$ . Here

$$\gamma = \frac{U_{NP} - NU_{bulk}}{4\pi r_{NP}^2} \quad [A \cdot 1]$$

Figure 13 shows that  $\gamma$  is not an intrinsic property of the NP, but it varies with particle size, independent of the force field. The value of  $\gamma$  for a 0.7 nm particle is approximately 3.6 J/m<sup>2</sup>, but drops to a stable value at large particle sizes (>2.5 nm) of 2.15 J/m<sup>2</sup> (COMB) or 2.52 J/m<sup>2</sup> (EAM). The variation of  $\gamma$  is the highest in the relevant size range of NP in PEMFC (1–3 nm). Similar behavior is observed if  $\gamma$  is calculated in units of [eV/atom] by replacing the denominator in Eq. 20 by the number of surface atoms in the NP (data not shown). The coupling between  $\gamma$  and particle size aligns with previous reports on crystalline NPs.<sup>33,40</sup> Such ambiguity in evaluating  $\gamma$  bring difficulty is supporting continuum models of NPs evolution by atomistic simulations.

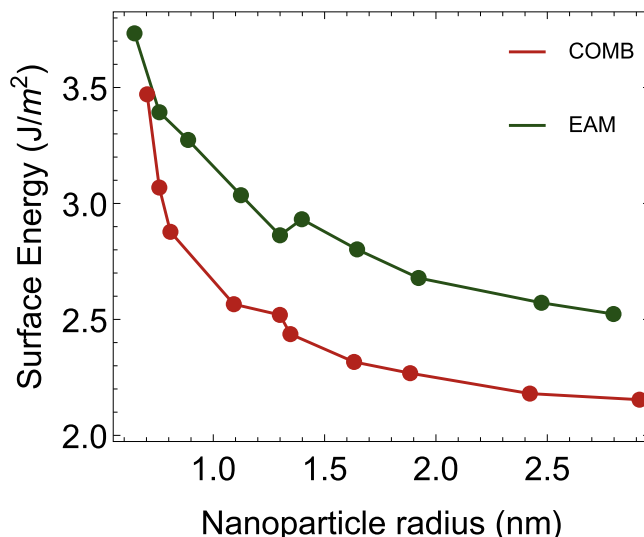


**Figure 13.** Direct evaluation of Pt NP surface energy  $\gamma$  shows a dependence on NP size. The coupling between  $\gamma$  and  $r_{NP}$  becomes ambiguous when being employed in continuum level theories.

## ORCID

Giovanna Bucci <https://orcid.org/0000-0001-7318-8225>

## References

- U. DOE, "The fuel cell technologies office multi-year research, development, and demonstration plan." *Tech. rep., Technical report: US Department of Energy* (2016). <https://www.energy.gov/eere/fuelcells/downloads/hydrogen-and-fuel-cell-technologies-office-multi-year-research-development>.
- R. Borup et al., "Scientific aspects of polymer electrolyte fuel cell durability and degradation." *Chem. Rev.*, **107**, 3904 (2007).
- M. M. Mench, E. C. Kumbur, and T. N. Veziroglu, *Polymer Electrolyte Fuel Cell Degradation* (Academic, New York) (2011).
- J. C. Meier, C. Galeano, I. Katsounaros, J. Witte, H. J. Bongard, A. A. Topalov, C. Baldizzone, S. Mezzavilla, F. Schüth, and K. J. Mayrhofer, "Design criteria for stable Pt/C fuel cell catalysts." *Beilstein Journal of Nanotechnology*, **5**, 44 (2014).
- Y.-C. Park, H. Tokiwa, K. Kakinuma, M. Watanabe, and M. Uchida, "Effects of carbon supports on Pt distribution, ionomer coverage and cathode performance for polymer electrolyte fuel cells." *Journal of Power Sources*, **315**, 179 (2016).
- D. J. Myers, X. Wang, M. C. Smith, and K. L. More, "Potentiostatic and potential cycling dissolution of polycrystalline platinum and platinum nano-particle fuel cell catalysts." *J. Electrochem. Soc.*, **165**, F3178 (2018).
- J. A. Gilbert, N. N. Kariuki, X. Wang, A. J. Kropf, K. Yu, D. J. Groom, P. J. Ferreira, D. Morgan, and D. J. Myers, "Pt catalyst degradation in aqueous and fuel cell environments studied via in-operando anomalous small-angle x-ray scattering." *Electrochimica Acta*, **173**, 223 (2015).
- P. Ferreira et al., "Instability of Pt/C electrocatalysts in proton exchange membrane fuel cells: a mechanistic investigation." *J. Electrochem. Soc.*, **152**, A2256 (2005).
- C. T. Campbell, S. C. Parker, and D. E. Starr, "The effect of size-dependent nanoparticle energetics on catalyst sintering." *Science*, **298**, 811 (2002).
- C. T. Campbell, S. C. Parker, and D. E. Starr, "The effect of size-dependent nanoparticle energetics on catalyst sintering." *Science*, **298**, 811 (2002).
- I. M. Lifshitz and V. V. Slyozov, "The kinetics of precipitation from supersaturated solid solutions." *J. Phys. Chem. Solids*, **19**, 35 (1961).
- C. Wagner, "Theorie der alterung von niederschlägen durch umlösen (ostwald-reifung)." *Zeitschrift für Elektrochemie, Berichte der Bunsengesellschaft für physikalische Chemie*, **65**, 581 (1961).
- M. K. Chen and P. W. Voorhees, "The dynamics of transient ostwald ripening." *Model. Simul. Mater. Sci. Eng.*, **1**, 591–612 (1993).
- P. Voorhees, G. McFadden, R. Boisvert, and D. Meiron, "Numerical simulation of morphological development during ostwald ripening." *Acta Metall.*, **36**, 207 (1988).
- R. K. Ahluwalia, S. Arisetty, J.-K. Peng, R. Subbaraman, X. Wang, N. Kariuki, D. J. Myers, R. Mukundan, R. Borup, and O. Polevaya, "Dynamics of particle growth and electrochemical surface area loss due to platinum dissolution." *J. Electrochem. Soc.*, **161**, F291 (2014).

**Table A-I. Data-structure for the network model.**

Information	
Vertex	<ol style="list-style-type: none"> <li>its set of satellites</li> <li>whether there is a particle there or not</li> <li>the particle radius</li> <li>its location</li> <li>the number of moles of ions in solution (dissolved from the solid particle)</li> </ol>
Satellite	<ol style="list-style-type: none"> <li>the vertex that owns it</li> <li>the edge it is connected to</li> <li>its partner satellite. Two partner satellites belong to the same edge and to different particles</li> <li>the list of other satellites in the same orbit (belonging to the same vertex)</li> <li>the angle between the satellite and all other satellites on the same particle. The angle is defined on the great-circle between the centers of each satellite pair</li> <li>the fraction of the spherical shell (surrounding the vertex) that it owns</li> <li>the relative extension of the border with all its neighbouring satellites</li> <li>the number of moles it contains</li> </ol>
Edge	<ol style="list-style-type: none"> <li>the two satellites that it is connected to</li> <li>the vertices that it is connected to via its satellites</li> <li>its length</li> <li>the steady state concentration gradient along the edge</li> <li>the flux direction</li> </ol>

16. H. A. Baroody, D. B. Stolar, and M. H. Eikerling, "Modelling-based data treatment and analytics of catalyst degradation in polymer electrolyte fuel cells." *Electrochimica Acta*, **283**, 1006 (2018).
17. K. Yu, D. J. Groom, X. Wang, Z. Yang, M. Gummalla, S. C. Ball, D. J. Myers, and P. J. Ferreira, "Degradation mechanisms of platinum nanoparticle catalysts in proton exchange membrane fuel cells: The role of particle size." *Chemistry of Materials*, **26**, 5540 (2014).
18. W. R. Inc, *Mathematica, Version 12.1* (Champaign, IL) (2020).
19. H. Sato, M. Yui, and H. Yoshikawa, "Ionic diffusion coefficients of  $\text{Cs}^+$ ,  $\text{Pb}^{2+}$ ,  $\text{Sm}^{3+}$ ,  $\text{Ni}^{2+}$ ,  $\text{SeO}_4^{2-}$  and  $\text{TeO}_4^{2-}$  in free water determined from conductivity measurements." *J. Nucl. Sci. Technol.*, **33**, 950 (1996).
20. S. Schneider, A. Surrey, D. Pohl, L. Schultz, and B. Rellinghaus, "Atomic surface diffusion on pt nanoparticles quantified by high-resolution transmission electron microscopy." *Micron*, **63**, 52 (2014), David J.H. Cockayne.
21. M. Pourbaix, *Atlas of electrochemical equilibria in aqueous solutions* (Pergamon, Oxford, New York) (1966).
22. Y. Shao-Horn, W. Sheng, S. Chen, P. J. Ferreira, E. Holby, and D. Morgan, "Instability of supported platinum nanoparticles in low-temperature fuel cells." *Topics in Catalysis*, **46**, 285 (2007).
23. J. Taylor, "li-mean curvature and weighted mean curvature." *Acta Metallurgica et Materialia*, **40**, 1475 (1992).
24. S. Plimpton, "Fast parallel algorithms for short-range molecular dynamics." *J. Comput. Phys.*, **117**, 1 (1995).
25. X. Zhou, R. Johnson, and H. Wadley, "Misfit-energy-increasing dislocations in vapor-deposited co/nife multilayers." *Phys. Rev. B*, **69**, 144113 (2004).
26. A. C. Antony, T. Liang, and S. B. Sinnott, "Nanoscale structure and dynamics of water on pt and cu surfaces from md simulations." *Langmuir*, **34**, 11905 (2018).
27. A. Antony, S. Akhade, Z. Lu, T. Liang, M. Janik, S. Phillpot, and S. Sinnott, "Charge optimized many body (comb) potentials for pt and au." *J. Phys.: Condens. Matter*, **29**, 225901 (2017).
28. V. Fiorentini and M. Methfessel, "Extracting convergent surface energies from slab calculations." *J. Phys.: Condens. Matter*, **8**, 6525 (1996).
29. W. Luo, W. Hu, K. Su, and F. Liu, "The calculation of surface free energy based on embedded atom method for solid nickel." *Appl. Surf. Sci.*, **265**, 375 (2013).
30. Y. Qi, T. Çağın, W. L. Johnson, and W. A. Goddard III, "Melting and crystallization in ni nanoclusters: The mesoscale regime." *The Journal of Chemical Physics*, **115**, 385 (2001).
31. J. C. Hamilton, "Edge energies: Atomistic calculations of a continuum quantity." *Phys. Rev. B*, **73**, 125447 (2006).
32. C. L. Cleveland and U. Landman, "The energetics and structure of nickel clusters: Size dependence." *The Journal of chemical physics*, **94**, 7376 (1991).
33. J. Wang, J. Bian, X. Niu, and G. Wang, "A universal method to calculate the surface energy density of spherical surfaces in crystals." *Acta Mechanica Sinica*, **33**, 77 (2017).
34. R. M. Darling and J. P. Meyers, "Kinetic Model of Platinum Dissolution in PEMFCs." *J. Electrochem. Soc.*, **150**, A1523 (2003).
35. R. K. Ahluwalia, D. D. Papadias, N. N. Kariuki, J.-K. Peng, X. Wang, Y. Tsai, D. G. Graczyk, and D. J. Myers, "Potential Dependence of Pt and Co Dissolution from Platinum-Cobalt Alloy PEFC Catalysts Using Time-Resolved Measurements." *J. Electrochem. Soc.*, **165**, F3024 (2018).
36. R. K. Ahluwalia, S. Arisetty, X. Wang, X. Wang, R. Subbaraman, S. C. Ball, S. DeCrane, and D. J. Myers, "Thermodynamics and kinetics of platinum dissolution from carbon-supported electrocatalysts in aqueous media under potentiostatic and potentiodynamic conditions." *J. Electrochem. Soc.*, **160**, F447 (2013).
37. G. S. Harzer, J. N. Schwämmlein, A. M. Damjanović, S. Ghosh, and H. A. Gasteiger, "Cathode loading impact on voltage cycling induced PEMFC degradation: A voltage loss analysis." *J. Electrochem. Soc.*, **165**, F3118 (2018).
38. L. Ratke and P. W. Voorhees, *Growth and Coarsening. Ostwald Ripening in Material Processing* (Springer, Berlin, Heidelberg) (2002).
39. F. M. Ross, *Liquid Cell Electron Microscopy* (Cambridge University Press, Cambridge) (2016).
40. Y. Wei and S. Chen, "Size-dependent surface energy density of spherical face-centered-cubic metallic nanoparticles." *Journal of nanoscience and nanotechnology*, **15**, 9457 (2015).